

See discussions, stats, and author profiles for this publication at: <https://www.researchgate.net/publication/330801885>

Estimation of state of health of lithium-ion batteries based on charge transfer resistance considering different temperature and state of charge

Article in *The Journal of Energy Storage* · February 2019

DOI: 10.1016/j.est.2018.11.020

CITATIONS

51

READS

1,139

3 authors, including:



Xueyuan Wang

Tongji University

25 PUBLICATIONS 207 CITATIONS

[SEE PROFILE](#)



Haifeng Dai

Tongji University

134 PUBLICATIONS 2,047 CITATIONS

[SEE PROFILE](#)

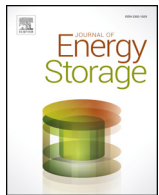
Some of the authors of this publication are also working on these related projects:



National Key Scientific Instrument and Equipment Development Project (No.2012YQ15025603) [View project](#)



NSFC : Research on AC heating mechanism and method of Lithium-ion power battery at low temperature [View project](#)



Estimation of state of health of lithium-ion batteries based on charge transfer resistance considering different temperature and state of charge

Xueyuan Wang^{a,b}, Xuezhe Wei^{a,b,*}, Haifeng Dai^{a,b}

^a Clean Energy Automotive Engineering Center, Tongji University, 4800 Caoan Road, Shanghai, China

^b School of Automotive Studies, Tongji University, 4800 Caoan Road, Shanghai, China

ARTICLE INFO

Keywords:

Lithium-ion battery
State of health
Electrochemical impedance spectroscopy
Charge transfer resistance
Temperature
State of charge

ABSTRACT

State of health diagnosis and estimation of lithium-ion batteries is a key feature of an advanced battery management system. Electrochemical impedance spectroscopy is frequently used for the state of health diagnosis and estimation. In the paper, the charge transfer resistance of the battery is obtained by fitting the impedance spectroscopy with an equivalent impedance model to estimate state of health. And an analytical calculation model with temperature and state of charge as inputs is derived and verified considering their effect on the charge transfer resistance. With the calculation model, the charge transfer resistance at randomly selected state of charge and temperature is converted to the standard state to be comparable for the state of health estimation. It is indicated that state of health estimated with the converted and the direct fitted charge transfer resistance agree well. The battery state of health estimation method with the converted charge transfer resistance eliminates the need to specifically control the temperature and state of charge during the impedance spectrum measurement. It benefits the practical application of the state of health estimation with electrochemical impedance spectroscopy.

1. Introduction

The performance improvement of Electric Vehicles (EVs) and the continuous development of the EV market scale put forward higher requirements for Battery Management Systems (BMSs). During a practical application, the aging process of on-board power lithium-ion battery pack is accompanied by the degradation of its performance. It directly attenuates output power of the battery pack or shortens driving range of an EV. Diagnosis and estimation of the aging state becomes a necessary feature of an advanced BMS. It contributes to an efficient and safe application of the power lithium-ion batteries.

At present, many State of Health (SOH) diagnosis and estimation methods for lithium-ion batteries are proposed. Data-driven aging state estimation methods such as neural network and support vector machine do not rely on battery models to estimate the aging state [1,2]. However, obtaining an effective training set is difficult. The operating conditions of the power battery are complicated. The training of specific working conditions makes the adaptability of the method worse, which leads to large error in practical applications. Relatively speaking, the estimation method based on the equivalent circuit model is more advantageous. Genetic algorithm, Kalman filter, least square method and other improved state estimation methods are used to estimate the

capacity and the internal resistance online to quantify SOH [3–7]. The model based method can provide the internal resistance and the capacity of the battery on line by fitting the terminal voltage and the current. However, as a nonlinear chemical system, the model parameters identified with the dynamic current and voltage are not precise and accurate.

In order to diagnose the changes in the battery electrode processes, Electrochemical Impedance Spectroscopy (EIS) is applied to diagnose the aging state and estimate SOH. It is a kind of quasi-state method to present the electrode processes more confidently. Film formation, charge transfer on the electrode and electrolyte interface and diffusion in the solid particles can be investigated with EIS [8,9]. However, the process inside a battery cell, i.e. the electronic/ionic conduction and the lithium-ion insertion/extraction reaction, are always affected by the varying temperature and State of Charge (SOC). As a result, EIS reflecting these processes is also affected by temperature and SOC [10–12]. These factors must be taken into account and excluded in the diagnosis and estimation of the aging state of the battery using EIS. As far as the authors know, the effect of temperature and SOC is rarely or not fully considered in previous studies. Yuan et al. studied the relationship between the charge transfer resistance and the battery aging state. They proposed to estimate the aging state with the resistance

* Corresponding author at: Clean Energy Automotive Engineering Center, Tongji University, 4800 Caoan Road, Shanghai, China.

E-mail address: weixzh@tongji.edu.cn (X. Wei).

without considering the effect of temperature and state of charge [13]. Stroe et al. fitted the lumped impedance model with EIS to obtain the variation of the model parameters with SOC and SOH. In order to exclude the effect of SOC, the ohmic resistance was finally selected to estimate the aging state [14]. Galeotti et al. studied the variation of the internal resistance with SOC and formed a map to consider the effect during SOH estimation with the internal resistance [15]. However, they did not consider the effect of temperature on the ohmic resistance. In fact, the effect of temperature on the ohmic resistance is also large compared to the effect of SOC. The neglect of temperature and SOC effect on the resistance limits the flexibility of using EIS for the battery aging state estimation. In order to overcome the shortcoming, the relationship between EIS of the lithium-ion battery and temperature and SOC is studied in the paper. Based on it, SOH estimation method of the battery considering temperature and SOC is finally proposed and verified. It is considered to be the biggest contribution of the paper for the estimation of SOH with EIS.

For state estimation with EIS, it is first necessary to obtain EIS board. The EIS measuring equipment used in the laboratory is expensive due to its wide measurement frequency range, high precision and versatility. It is possible to measure battery impedance for specific vehicular applications with a low-cost solution. In a distributed impedance measurement system, a unit mounted on battery cell injects perturbing signal into the battery cell separately. And the current and the response voltage are sampled locally to calculate the impedance [16,17]. In a centralized impedance measuring method, a high power DC-DC converter perturbs the battery module with a sinusoidal current. And then the current and the response voltage are measured locally and the battery impedance is calculated [18–20]. In order to shorten the measurement time, a square wave [21–23], a pseudo-random binary sequence [24,25] and a signal during a driving cycle [26] can be applied to calculate the battery impedance with Fast Fourier transform, time-sharing Fourier transform and wavelet transform processing the voltage and the current profiles. With the increasing number of on-board battery impedance spectrum measurement methods and devices proposed or implemented, diagnosing and estimating the battery SOH with EIS becomes more feasible.

The rest of the paper is organized as follows. The second section introduces the experimental setup to measure impedance spectra of the lithium-ion battery at different temperature, SOC and aging state. And then the measurement results are shown and discussed. The third section is about the parameter identification of the battery impedance model adopted to fit the impedance spectrum. The fourth section derives the analytic relationship between the charge transfer resistance and the battery state. The fifth section is about the estimation of the battery SOH with the charge transfer resistance considering different temperature and SOC. And in the sixth section the conclusions are drawn.

2. Study of electrochemical impedance spectrum at different temperature, state of charge and aging state

2.1. Experimental setup for impedance spectrum measurement

The battery used in the study is a prismatic LiFePO₄ battery cell typed with nominal capacity of 8 Ah. Maccor 4300 is used to measure the discharge capacity and perform the aging cycle on the battery cell. Impedance spectra are measured with the electrochemical workstation Solartron 1287/1255B with the power amplifier, Toyo Seiki PBi250-10. SOC is adjusted with the electrochemical workstation. The battery temperature is controlled by the ambient chamber TOTA T-TOP-C. The battery is cycled with 2C rate at 318 K (45°C) for acceleration. The whole test contains several sub-tests listed as follows. To obtain impedance spectra at different temperature and SOC after different aging cycles, Fig. 1 describes the basic test flow made up of the sub-tests.

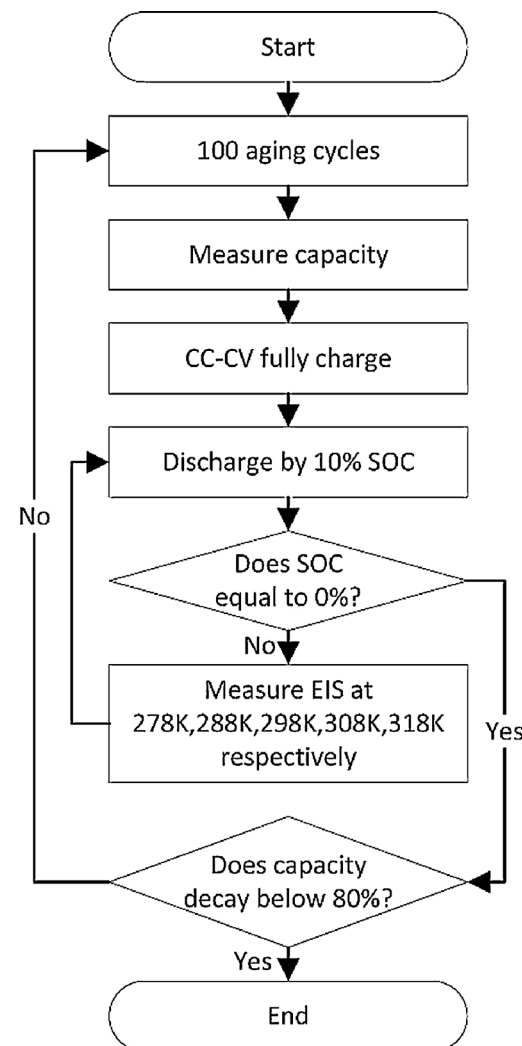


Fig. 1. Flow chart of the experiment.

A CC-CV charging

2.2. Results and discussions of measured impedance spectra

Fig. 2 shows the electrochemical impedance spectra measured at different temperature, SOC and number of aging cycles. Two arcs can be seen on the impedance spectrum. It is generally believed that the arc in the high frequency region is related to the impedance of the SEI film of the battery. And the slightly flat arc in the intermediate frequency region reflects the impedance of the charge transfer process of the battery electrodes [27–32]. In addition, the straight line segment in the low frequency region reflects the impedance of the diffusion process of lithium ions in the solid particles.

The electrochemical impedance spectra at 278 K–318 K (5°C–45°C) are plotted in Fig. 2(a). The change of temperature has a significant effect on the impedance spectra. It is seen that the two arcs presented on the impedance spectrum are obviously enlarged with the drop of the temperature from 318 K to 278 K. And the impedance spectra are also shifted rightwards indicating the ohmic resistance of the battery increases as the temperature decreases. The diffusion impedance in the low frequency range also increases obviously as the temperature drops. Fig. 2(b) shows the change of the impedance spectra of the battery when SOC varies from 10% to 90% at 298 K. It is indicated that the change of the high-frequency arc and the inductive segment of the spectrum is basically negligible due to SOC, and the arc appearing in

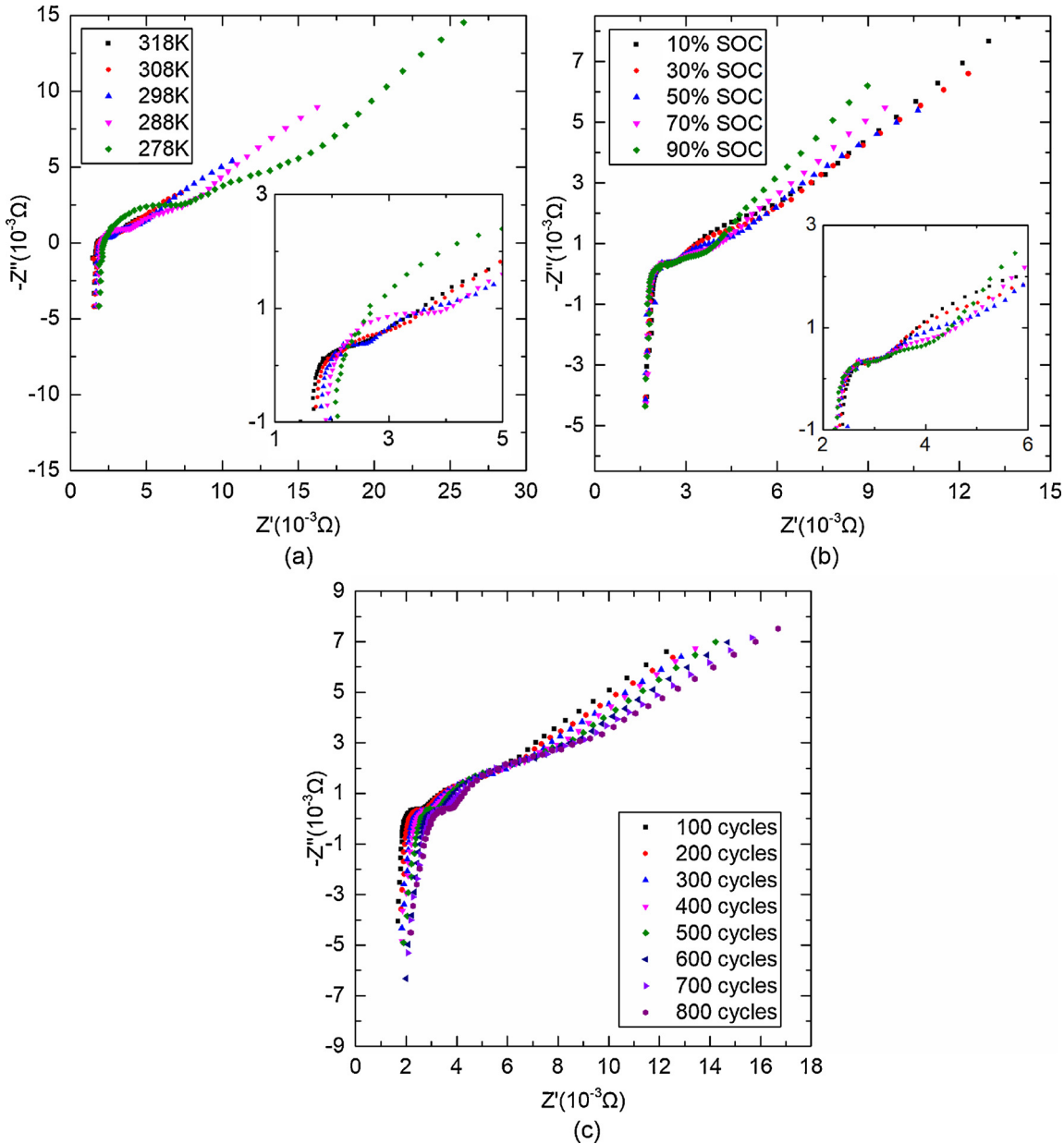


Fig. 2. Electrochemical impedance spectra measured at different temperature, State of Charge (SOC) and number of aging cycles.
 (a) Impedance spectra measured at different temperature, 50% SOC after 100 aging cycles; (b) impedance spectra measured at different SOC, 298 K after 100 aging cycles; (c) impedance spectra measured at 50% SOC and 298 K after different aging cycles.

the intermediate frequency region becomes larger and more significant as SOC decreases. The former indicates that SOC has little effect on the conductivity of the solid/electrolyte phase and the impedance of the SEI film. And the change of the second arc shows that the charge transfer resistance of the battery is greatly affected by SOC. Fig. 2(c) shows the electrochemical impedance spectra measured at 298 K and 50% SOC after the battery cell undergoes different aging cycles. There are three obvious characteristics changing with the number of aging cycles. (1) The impedance spectra of the battery gradually shift to the right, (2) the high frequency arc has a tendency to become smaller and (3) the intermediate frequency arc bigger. It is seen from the above experimental results that the ohmic resistance, the SEI film resistance and the charge transfer resistance are all affected by temperature or SOC. And the trends varies as the number of aging cycles increases.

3. Identification of battery impedance model parameters

3.1. Equivalent impedance model of battery

In order to further study the effect of battery state on the ohmic resistance, the SEI film resistance and the charge transfer resistance, an equivalent impedance model is used to fit the electrochemical impedance spectrum of the battery.

The applied impedance model is shown in Fig. 3 [33]. The first paralleled RC branch is used to describe the SEI film impedance. A constant phase element $Q_{\text{CPE}1}$ is introduced to represent the film capacitance considering the dispersion effect. And R_{film} is the film resistance. The second paralleled RC branch is to describe the electrode interface impedance. Another constant phase element $Q_{\text{CPE}2}$ describes the double layer capacitor also considering dispersion effect. R_{ct} represents the charge transfer resistance. The diffusion impedance of lithium ions in the electrode solid particles is represented by a Warburg

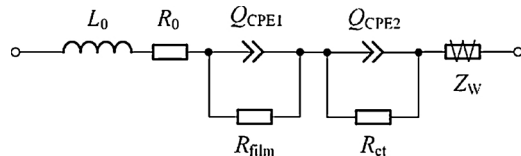


Fig. 3. Equivalent impedance model of lithium-ion batteries applied to fit electrochemical impedance spectrum.

element Z_W . A resistor R_0 is used to describe the electronic conductance characteristic of the solid phase material and the ionic conductance characteristic of the electrolyte phase. And the stray inductance introduced by the current collector and leads is lumped with an inductor L_0 .

In the equivalent impedance model, the impedance of the constant phase element Q_{CPE} has an expression represented by the following Eq. (1).

$$Z_{CPE} = \frac{1}{T_{CPE}(j\omega)^{p_{CPE}}} \quad (1)$$

Here, T_{CPE} and p_{CPE} are parameters of the constant phase element, j is the imaginary unit and ω is the angular frequency. The Warburg impedance Z_W is shown as Eq. (2) [34,35].

$$Z_W = R_W \frac{\tanh[(j\omega T_W)^{p_W}]}{(j\omega T_W)^{p_W}} \quad (2)$$

Here, R_W is Warburg coefficient expressed as Eq. (3) [36,37].

$$R_W = \frac{RT}{\sqrt{2}F^2\sqrt{D}c_0} \quad (3)$$

And T_W is defined as Eq. (4) [38].

$$T_W = \frac{l^2}{D} \quad (4)$$

D is the solid diffusion coefficient, c_0 is the initial lithium-ion concentration in solid particles, l is the effective diffusion thickness, R is the universal gas constant, F is the Faraday constant, T is the temperature and p_W is the parameter of the Warburg element. Here, p_W is set to a free value instead of a fixed value 0.5 to better fit the spectra in the low frequency range. According to the series or parallel connection form of the equivalent components in Fig. 3, the battery impedance is expressed as Eq. (5).

$$Z = j\omega L_0 + R_0 + \frac{R_{film}}{R_{film} T_{film} (j\omega)^{p_{film}} + 1} + \frac{R_{ct}}{R_{ct} T_{dl} (j\omega)^{p_{dl}} + 1} + R_W \frac{\tanh[(j\omega T_W)^{p_W}]}{(j\omega T_W)^{p_W}} \quad (5)$$

3.2. Identification method of impedance model parameters

The parameters of the equivalent impedance model to be determined are shown in Table 1. The approximate range of each impedance model parameter is listed by estimating and reviewing relevant references. For the LiFePO₄ battery used, the specific value of each parameter cannot be accurately obtained. Thus, it is easily affected by the given initial value and then leads to a local optimal solution if a parameter optimization method, e.g. the nonlinear least square method, is directly used. Therefore, a particle swarm optimization method is used to optimize the parameters to narrow the parameter range and give the initial value of the parameters for the later optimization. It has better global convergence and simple algorithm, which is quite suitable for the optimization problems.

The sum of the squared error of the impedance calculated and measured at certain frequency is used as the fitness function of the particle swarm algorithm as is shown in Eq. (6).

$$\min E = \sum_{i=1}^n (Z'_i - z'_i)^2 + \sum_{i=1}^n (Z''_i - z''_i)^2 \quad (6)$$

Here, n is the total number of the impedance at different frequency points, Z'_i and Z''_i are the real and the imaginary part of the impedance measured at a certain frequency, z'_i and z''_i are the real and the imaginary part of the impedance calculated with the equivalent impedance model. It is seen from Eq. (6) that the fitness function cannot distinguish the impedance in the high frequency or the low frequency range. Generally, the information contained in the medium and the high frequency is more abundant but the impedance value is smaller. The impedance model parameters obtained by the fitness function of the Eq. (6) are easily to cause large fitting error in the medium and high frequency range due to the small contribution of the small impedance value. Therefore, a weighting factor as Eq. (7) is introduced here to ensure better parameter optimization when the impedance is small in the medium and the high frequency range.

$$W_i = \frac{1}{Z'^2_i + Z''^2_i} \quad (7)$$

Accordingly, the fitness function finally adopted is shown as Eq. (8).

$$\min E = \sum_{i=1}^n W_i (Z'_i - z'_i)^2 + \sum_{i=1}^n W_i (Z''_i - z''_i)^2 \quad (8)$$

To avoid the particle swarm algorithm terminated at a local optimization solution, a chaotic search is added to the standard particle swarm optimization algorithm to improve the global optimal search ability. In actual implementation, if the optimal fitness is found to be unchanged for several consecutive times, it is considered that the algorithm may converge to a local optimum. Then the chaotic search is performed to find a globally better combination of parameters within the given parameter range. The chaotic search strategy uses the classic Logistic mapping as is shown in Eq. (9) to change the position of the parameters.

$$Y_{i+1} = \mu Y_i (1 - Y_i), \quad i=0, 1, 2, \dots \quad (9)$$

Here, Y_i is a chaotic variable that satisfies $0 < Y_i < 1$, and μ is a chaotic control variable. Fig. 4(a) shows that different behavior of the system described by Eq. (9) is observed with different value of the parameter μ ($2 \leq \mu \leq 4$). When $\mu = 4$, the system described by Eq. (9) is in a completely chaotic state as is shown in Fig. 4(b) [40].

At the completely chaotic state, a small change in the initial value Y_0 causes a huge change in Y_i . This feature helps particle swarm search jump out a possible local optimal solution. The chaotic variables and the model parameters are mapped as Eq. (10) and reversely as Eq. (11).

$$Y = \frac{x - X_{\min}}{X_{\max} - X_{\min}} \quad (10)$$

$$x = X_{\min} + Y(X_{\max} - X_{\min}) \quad (11)$$

Here, X_{\max} and X_{\min} are respectively the upper and the lower limit of the parameter x to be identified. If the optimal fitness changes by three times less than 0.001, it is considered that particle swarm optimization may fall into the local optimum. At this point, the chaotic search algorithm is invoked and accelerate the convergence to the global optimal solution. The key steps of the chaotic search algorithm are shown in Fig. 5. The value of the parameters obtained by the particle swarm optimization is used as the initial value to further optimize by the software ZView.

3.3. Identification results of impedance model parameters

The impedance in the frequency range of 0.01 Hz–1000 Hz is selected to identify the parameters of the equivalent impedance model. The battery impedance spectra change with the temperature, SOC and aging state. And the frequency related to the geometric characteristic

Table 1

Parameters of equivalent impedance model.

Symbol	Description	Unit	Value
L_0	Equivalent inductor	H	$10^{-8}\text{--}10^{-7}$ [39]
R_0	Equivalent ohmic resistor	Ω	$1 \times 10^{-3}\text{--}3 \times 10^{-3}$ ^a
R_{ct}	Charge transfer resistance	Ω	$1 \times 10^{-4}\text{--}1 \times 10^{-2}$ [39]
T_{dl}	Constant phase element 1	$\Omega^{-1}\text{s}^p(0 < p \leq 1)$	$0\text{--}200$ ^b
p_{dl}		—	$0\text{--}1$ ^b
R_{film}	Resistance of solid electrolyte interphase	Ω	$1 \times 10^{-4}\text{--}1 \times 10^{-2}$ [39]
T_{film}	Constant phase element 2	$\Omega^{-1}\text{s}^p(0 < p \leq 1)$	$0\text{--}10$ ^b
p_{film}		—	$0\text{--}1$ ^b
D	Diffusion coefficient in solid phase	m^2s^{-1}	$1 \times 10^{-16}\text{--}1 \times 10^{-19}$ [31]
l	Effective diffusion thickness	m	$1 \times 10^{-6}\text{--}1 \times 10^{-5}$
c_0	Initial concentration in solid phase	$\text{mol}\cdot\text{m}^{-3}$	$1 \times 10^4\text{--}1 \times 10^5$
R_w	Warburg element	Ω	$1 \times 10^{-4}\text{--}1 \times 10^{2c}$
T_w		s	$1 \times 10^4\text{--}1 \times 10^{9c}$
p_w		—	$0\text{--}1$ ^b

^a Estimated from the intersection of the impedance spectrum and the real axis.^b Parameter range is large enough.^c Estimated with Eqs. (3) and (4).

points on the impedance spectrum also changes slightly. Therefore, the frequency range is chosen high enough to 1000 Hz to ensure the ohmic resistance of the battery is covered and low enough to 0.01 Hz to ensure complete coverage of the arc related to the charge transfer resistance to be investigated. Based on the chaotic particle swarm method proposed above, the optimization is first performed within a given parameter range. In Fig. 6, after the fifth search by standard particle swarm optimization, the optimal fitness has not changed three times in succession. Therefore, a chaotic search was invoked during the sixth search (shown by a red circle). With the help of chaotic search, the optimal fitness of particle swarms converges quickly. The corresponding particle swarm optimization results are shown below.

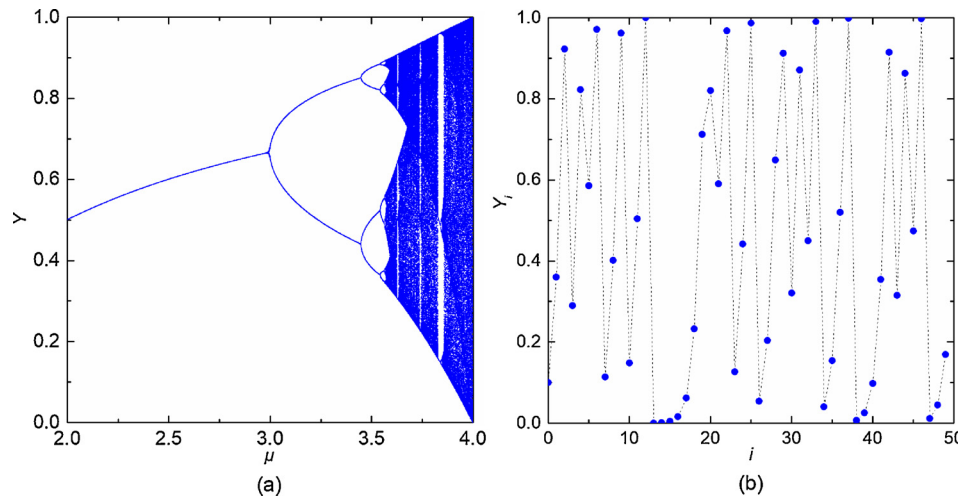
It can also be seen from Fig. 6 that the efficiency of the particle swarm method is relatively low in the later stage of optimizing the search. In order to accelerate the convergence, the initial value of the parameters obtained by the particle swarm method is given to a nonlinear optimization method such as the Levenberg-Marquardt method for subsequent parameter optimization. In the paper, the software Zview is applied to further optimize the parameters. The corresponding optimization results are shown in Fig. 7. As can be seen from the figure, the impedance model used has a quite good fit to EIS.

Fig. 8 shows the ohmic resistance R_0 , the SEI film resistance R_{film} and the charge transfer resistance R_{ct} obtained by fitting the impedance spectra at different temperature, SOC and aging state. In general, R_0 ,

R_{film} and R_{ct} show a certain regularity with the change of the battery state. (a)-(c) indicate that R_0 , R_{film} and R_{ct} all decrease as the battery temperature goes up. (d) and (f) show that R_0 and R_{ct} decrease as the battery SOC increases. (e) indicates that R_{film} has a tendency to decrease and then increase as SOC increases. (g) and (i) show that R_0 and R_{ct} gradually grow as the battery aging process continues, while R_{film} is steadily decreasing as is shown in (h).

The mechanism of effect of SOC and temperature on R_0 , R_{film} and R_{ct} is not exactly the same. For R_0 and R_{film} , the value is mainly affected by the conductivity of the solid phase or liquid phase. And for R_{ct} , its value is mainly affected by the rate of chemical reaction [41]. SOC and temperature have different effects on conductivity and chemical reaction rate. The effect of SOC on R_0 and R_{film} is also reflected in [12,42,43]. Similar experimental results of the effect of SOC on the charge transfer resistance are also mentioned in [35,44,45]. The relationship between temperature and resistance is described by the Arrhenius equation [41]. The resistance becomes smaller when the temperature rises as is shown in Fig. 9. In the figure, the slope of the line is considered to be related to the reaction activation energy. For R_{ct} , it is seen from Fig. 10 that the reaction activation energy does not substantially change with SOC and aging state of the battery. This is especially important for establishing a general relationship between R_{ct} and temperature which is applicable at different SOC and aging state.

The increase of the charge transfer resistance with the aging cycles

**Fig. 4.** Properties of Logistic map.(a) Different Y obtained with Eq. (9) as the value of μ changes from 2 to 4; (b) Different Y obtained with Eq. (9) as $\mu = 4$.

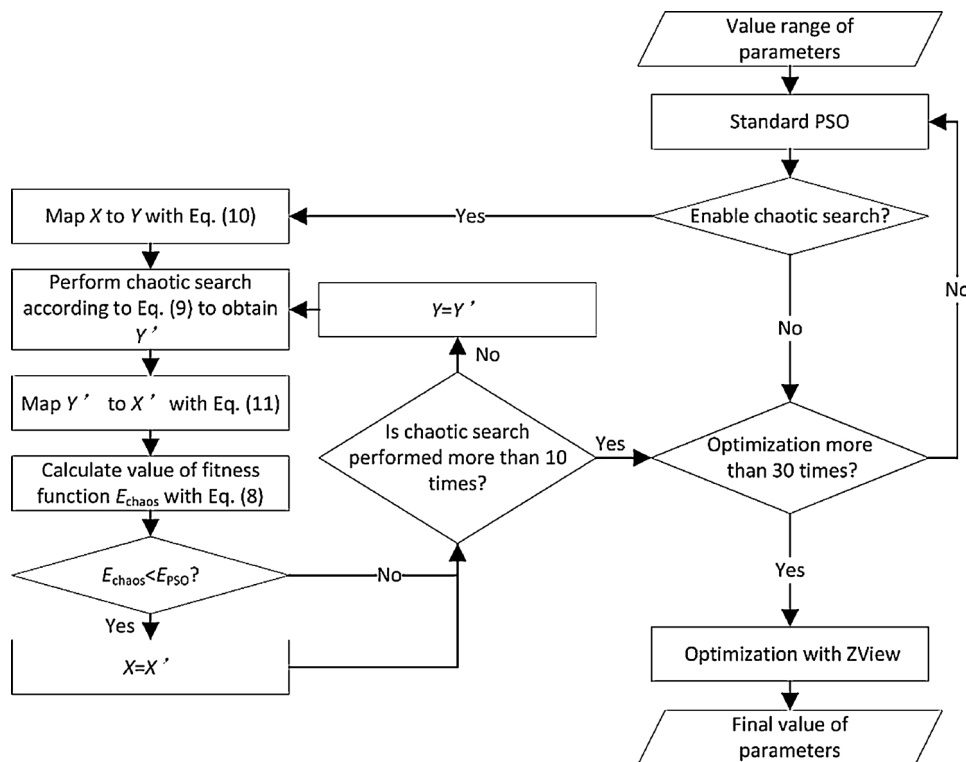


Fig. 5. Flow chart of identification of impedance model parameters.

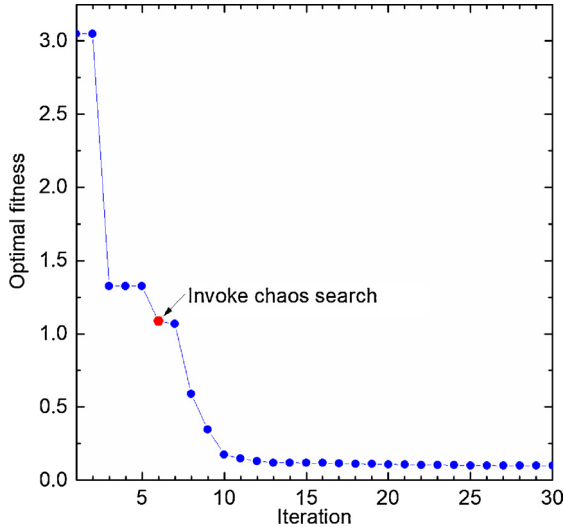


Fig. 6. Change of fitness of the chaos search based particle swarm optimization.

is closely related to the loss of the active lithium ions in the battery as is shown in Fig. 11. The irreversible loss of lithium ions reduces the chemical reaction rate for the lithium-ion concentration is reduced, which makes the charge transfer process more difficult [46,47]. The ohmic resistance also increases due to the close of the electronic conduction paths caused by the collapse of the electrode structures and the decrease of the ionic conductivity of the electrolyte because of the consumption of the active lithium ions [48]. In general, SEI film is likely to continue to grow and thicken as the battery is aged. However, the growth of the SEI film does not mean that R_{film} always increases. Conversely, the decrease in R_{film} with ageing is also a common change. This phenomenon is caused by the fact that the SEI composition at high temperature and high current density is different from the original composition, and the new composition has higher ionic conductivity.

For the LiPF6-ethylene carbonate/diethyl carbonate electrolyte used, Lee et al. found that Li_2CO_3 with higher conductivity in the SEI film formed at high temperature is produced more than ROCO_2Li , which leads to decrease in the resistance of the film to lithium ions [49]. M. Dollé et al. found that high current density also increases Li_2CO_3 with higher conductivity, which in turn leads to a decrease in SEI film resistance [50]. Similar conclusions are also raised in [28,29,30–53]. The growth mechanism of the SEI film indicates that the composition of the film changes as the operating conditions change, making the SEI film resistance not universal to estimate the aging state of the battery. Therefore, R_{film} is not used as an indicator of SOH in the paper.

When the temperature goes up to 318 K, the value of R_{ct} is reduced to 1/10 of that at 278 K. And R_{ct} decreases to 1/3 of that at 10% SOC when SOC increases to 90%. Besides, the value of R_{ct} grows to three times greater than that after 100 cycles as the number of aging cycles continually increases from 100 to 800. It is seen that R_{ct} changes more significantly and the regularity is more obvious comparing to the trend of R_0 with temperature and SOC. Therefore, it is more appropriate to use the charge transfer resistance to estimate the battery SOH.

4. Calculation model of charge transfer resistance considering temperature and state of charge

4.1. Derivation of calculation model

In order to analytically express the relationship between the charge transfer resistance and the battery state, i.e. temperature and SOC, a calculation model is derived in the section considering the dynamic of the electrode processes. The interfacial reaction dynamic of the electrodes is based on the relationship between the faradaic current and the electrode over potential which is known as Butler-Volmer equation. It is expressed as Eq. (12).

$$j_{\text{fd}} = j_0 \left(\exp\left(\frac{\alpha F}{RT}\eta\right) - \exp\left(\frac{-(1-\alpha)F}{RT}\eta\right) \right) \quad (12)$$

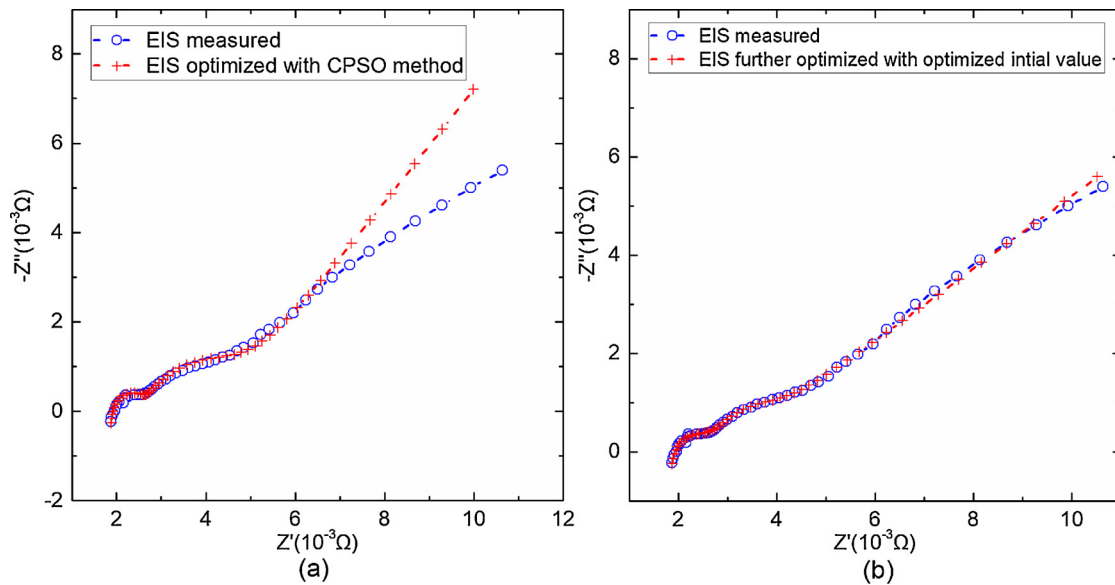


Fig. 7. Electrochemical Impedance Spectroscopy (EIS) optimized and measured.

- (a) EIS calculated with parameters optimized with chaotic particle swarm optimization method (CPSO);
(b) EIS calculated with parameters further optimized based on the initial value obtained with CPSO.

Here, j_{fd} is the faradaic current density on the surface of the electrode, α is the transfer coefficient and η is the over potential. j_0 is the exchange current density and is expressed as Eq. (13) with the temperature-dependent reaction rate constant k_0 , the maximum lithium-ion concentration of the electrode solid particles c_{\max} , the lithium-ion concentration in electrolyte c_e and the charge state of the electrode θ [46].

$$j_0 = k_0 c_{\max} \sqrt{c_e \theta (1 - \theta)} \quad (13)$$

According to the Arrhenius' law, the relationship between the electrochemical reaction rate constant k_0 and temperature is shown in Eq. (14).

$$k_0 = A \exp\left(-\frac{E_a}{RT}\right) \quad (14)$$

Here, E_a is the chemical reaction activation energy. It is a constant irrespective of temperature, SOC and aging state as is analyzed previously.

Since the electrochemical impedance spectrum is measured at a kind of quasi-steady state, Eq. (12) can be linearized with the first order Taylor expansion at the corresponding battery operating point expressed as Eq. (15).

$$j_{fd} = j_0 \frac{F}{RT} \eta \quad (15)$$

Therefore, the charge transfer resistance can be obtained as Eq. (16).

$$R_{ct} = \frac{\Delta\eta}{\Delta j_{fd}} = \frac{RT}{Fj_0} \quad (16)$$

Substituting Eq. (13) and Eq. (14) into Eq. (16) yields the expression of R_{ct} as Eq. (17).

$$R_{ct} = \frac{R}{F A c_{\max} \sqrt{c_e}} \cdot \frac{T}{\exp\left(-\frac{E_a}{RT}\right) \sqrt{\theta(1 - \theta)}} \quad (17)$$

It is generally believed that the mid/low-frequency impedance of lithium-ion batteries is mainly provided by the positive electrode [54,55]. Therefore, the contribution of the negative electrode on the charge transfer resistance is no longer considered to simplify the analysis here. This simplification proves reasonable in the subsequent experimental results. And Eq. (17) is modified to better fit the effect of

SOC on R_{ct} . The relationship between the charge transfer resistance and the battery state, i.e. temperature and SOC, is obtained as Eq. (18). α_1 , β_1 and β_2 are parameters that need to be determined.

$$R_{ct} = \frac{\alpha_1 T \exp\left(\frac{\alpha_2}{T}\right)}{\sqrt{SOC^2 + \beta_1 SOC + \beta_2}} \quad (18)$$

4.2. Determination of calculation model parameters

In this section, the model parameters will be determined separately based on the relationship to temperature and SOC. In order to determine the specific relationship between R_{ct} and temperature, the term related to the battery SOC is represented by the parameter m . Therefore, Eq. (18) can be converted into Eq. (19).

$$R_{ct} = m T \exp\left(\frac{\alpha_2}{T}\right) \quad (19)$$

Using this equation to fit the trend of R_{ct} with temperature in Fig. 8(c), the result shown in Fig. 12(a) is obtained. The red line is calculated by Eq. (19) with $m = 3.3997 \times 10^{-16}$ and $\alpha_2 = 6667.88$. Since α_2 is related to the reaction activation energy of the electrode process, it is considered to be unchanged with the state of the battery. And m is related to the maximum lithium-ion concentration of the electrode solid particles and SOC of the battery. Therefore, m has different value at different SOC and SOH.

To further determine the parameters α_1 , β_1 and β_2 in Eq. (18), the temperature-dependent term is represented by a parameter n . Thus, the relationship between R_{ct} and SOC is obtained and shown in Eq. (20).

$$R_{ct} = \frac{n}{\sqrt{SOC^2 + \beta_1 SOC + \beta_2}} \quad (20)$$

Eq. (20) is used to fit the trend of R_{ct} with SOC in Fig. 8(f). The result is shown in Fig. 12(b). The red line is the fitting result with $n = 4.2458 \times 10^{-4}$, $\beta_1 = 0.3303$ and $\beta_2 = 0.0338$. Referring to Eq. (18), the parameter n has the expression shown in Eq. (21).

$$n = \alpha_1 T \exp\left(\frac{\alpha_2}{T}\right) \quad (21)$$

In the foregoing, $\alpha_2 = 6667.88$ is obtained by fitting the trend of R_{ct} changing with temperature. And the temperature is $T = 298$ K when the

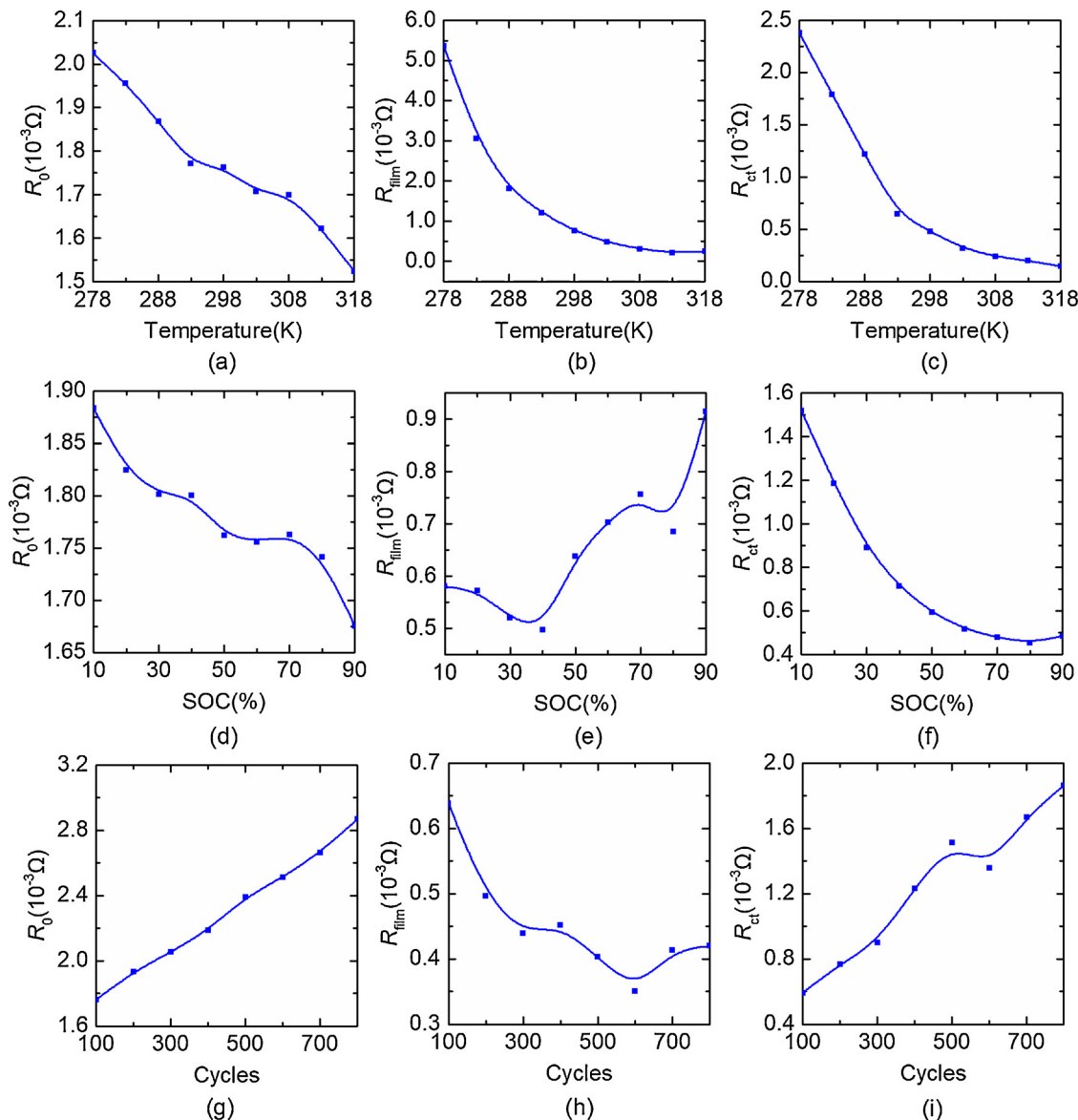


Fig. 8. The battery ohmic resistance R_o , the SEI film resistance R_{film} and the charge transfer resistance R_{ct} at different state obtained by fitting the equivalent impedance model.

(a)-(c) R_o , R_{film} and R_{ct} obtained at different temperature and 70% State of Charge (SOC) after 100 aging cycles; (d)-(f) R_o , R_{film} and R_{ct} obtained at different SOC and 298 K after 100 aging cycles; (g)-(i) R_o , R_{film} and R_{ct} obtained at 298 K and 50% SOC after different aging cycles.

relationship of R_{ct} and SOC is fitted. Substituting it into Eq. (21), $\alpha_1 = 2.7303 \times 10^{-16}$ is obtained. So far, the parameters α_1 , α_2 , β_1 and β_2 of the calculation model of the charge transfer resistance R_{ct} are finally determined.

To verify the calculation model, the combinations of different temperature and SOC are substituted into Eq. (18) to calculate the charge transfer resistance. And the true charge transfer resistance is also obtained by fitting impedance spectra at the same state. The relative error distribution of the charge transfer resistance obtained by the two methods is shown in Fig. 13. In Fig. 13(a), it is indicated that the relative error between the charge transfer resistance calculated by Eq. (18) and the direct fitted value is 14.7% or less in a wide temperature and SOC range. Especially at 298 K, the relative error is less than 6.3% when SOC is less than 80%. At different aging state, the model can still have an accurate prediction after recalculating α_1 . The error of the calculation results shown in Fig. 13(b-d) are acceptable in the SOC range lower than 70%.

5. Estimation of battery state of health based on charge transfer resistance

5.1. Change of charge transfer resistance after different aging cycles

As mentioned above, the charge transfer resistance of the battery exhibits a monotonously increasing trend as the battery is aged. In order to more intuitively see how the charge transfer resistance changes with battery life degradation, growth rate of the charge transfer resistance shown in Eq. (22) is introduced.

$$\delta = \frac{R_{ct} - R_{ct,fresh}}{R_{ct,fresh}} \times 100\% \quad (22)$$

Here, $R_{ct,fresh}$ is the reference value for calculating the growth rate of the charge transfer resistance. It refers to the value of the charge transfer resistance of the battery after 100 aging cycles.

Fig. 14 shows the trend of the growth rate of the charge transfer resistance at different temperature and SOC as the aging cycle

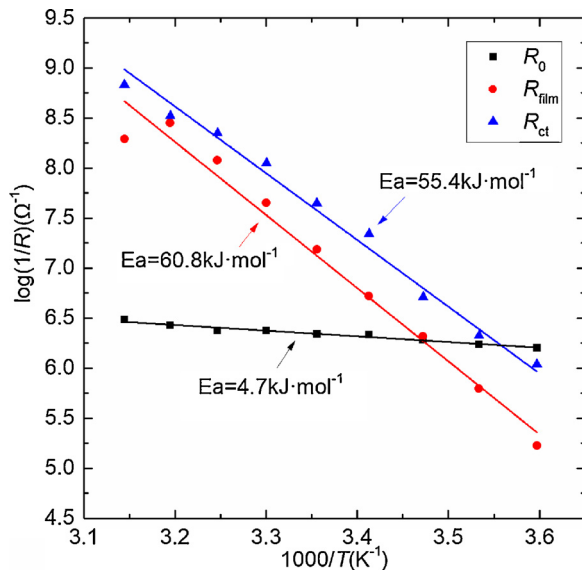


Fig. 9. Temperature dependence of R_0 , R_{film} and R_{ct} at 70% state of charge (SOC) after 100 aging cycles.

increases. The growth rate shown in the figure all exceeds 100% as the aging cycle increases to 800. And the lower the temperature or the lower SOC is, the bigger growth rate the transfer resistance has. It indicates that the performance degradation of the battery at low temperature and low SOC is more obvious as the battery life decays. Specifically, the growth rate of the charge transfer resistance obtained at 288 K or 50% SOC exceeds 200%. And it is worth noting that the curves obtained at different battery state are different. The effect of the battery SOC on the growth rate curve of the charge transfer resistance is significant from the beginning to the end of the aging process. However, the effect of the battery temperature on the growth rate is not as obvious as SOC, which is mainly reflected in the late aging process.

(a) Growth rate of R_{ct} at 288 K and 308 K at 50% SOC; (b) Growth rate of R_{ct} at 50% and 70% SOC at 298 K.

Because the aging of the battery is a long-term process. For on-board power batteries, the trend of aging is appreciable after a few months. And the aging process can last for several years. However, the temperature and SOC change in each charge and discharge cycle showing a

shorter time scale. The effect of the battery temperature and SOC on the charge transfer resistance is regarded as the noise during the SOH estimation, which needs to be filtered out.

5.2. Conversion of charge transfer resistance between different temperature and state of charge

In order to estimate the battery SOH over a long period of time, it is necessary to make the charge transfer resistance obtained at different state comparable. In this paper, the charge transfer resistance of the battery at different temperature and SOC is converted to a certain standard state by using Eq. (18), so that the charge transfer resistance of each aging state is comparable at uniform temperature and SOC. The state of the battery at 298 K and 50% SOC is set as the standard state. Correspondingly, we have the standard $T_{\text{std}} = 298$ K and $SOC_{\text{std}} = 0.5$. The following describes in detail how to convert the charge transfer resistance obtained at any temperature and SOC to the standard state.

It is assumed that α_2 , β_1 and β_2 in Eq. (18) are unchanged and α_1 is regarded as a variable at different aging state. This assumption has been used in the previous fitting of the parameters in Eq. (18). The experimental results also show the assumption is reasonable. In order to achieve effective charge transfer resistance conversion at different aging state, it is necessary to correct the influence of the aging state on the parameter α_1 . Then, the battery charge transfer resistance at the standard state can be calculated by the corrected calculation model of the charge transfer resistance. With the method, the charge transfer resistance is converted from any state to the standard state, and thus provide a basis for battery SOH estimation. The specific steps are as follows.

(1) The model to calculate the charge transfer resistance is shown as Eq. (23).

$$R_{\text{ct}} = f(T, SOC) = \frac{\alpha_1 T \exp\left(\frac{\alpha_2}{T}\right)}{\sqrt{SOC^2 + \beta_1 SOC + \beta_2}} \quad (23)$$

(2) The charge transfer resistance $R_{\text{ct},0}$ is obtained by fitting the impedance spectrum at T_0 and SOC_0 . By substituting $T = T_0$ and $SOC = SOC_0$ in Eq. (23), the calculated charge transfer resistance R_{ct} is obtained. Then the correction factor is expressed as Eq. (24).

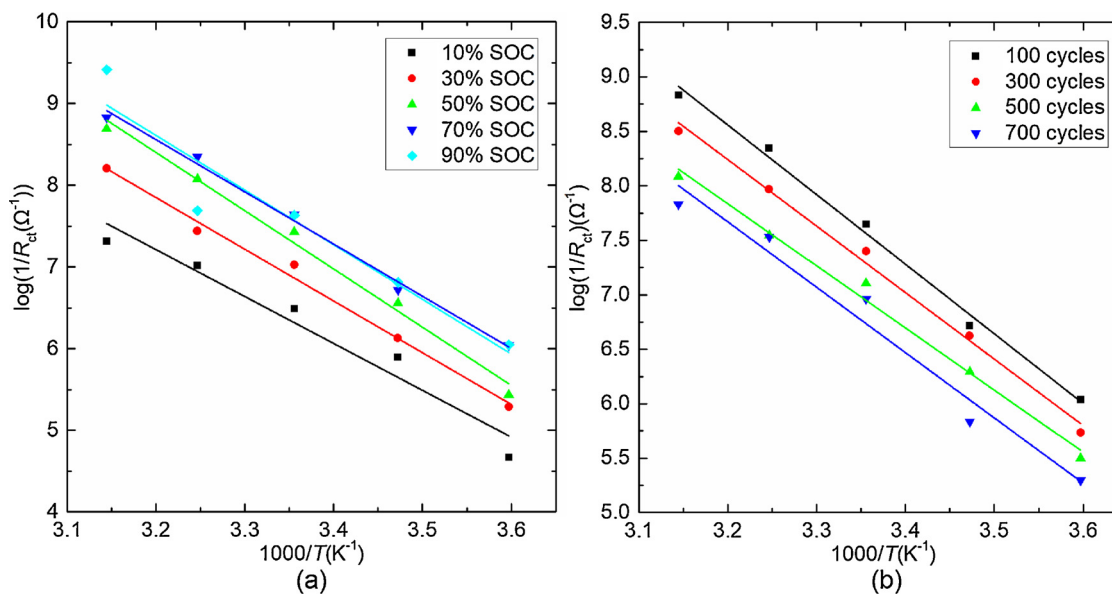


Fig. 10. Temperature dependence of R_{ct} (a) at different state of charge (SOC) and (b) after different aging cycles.

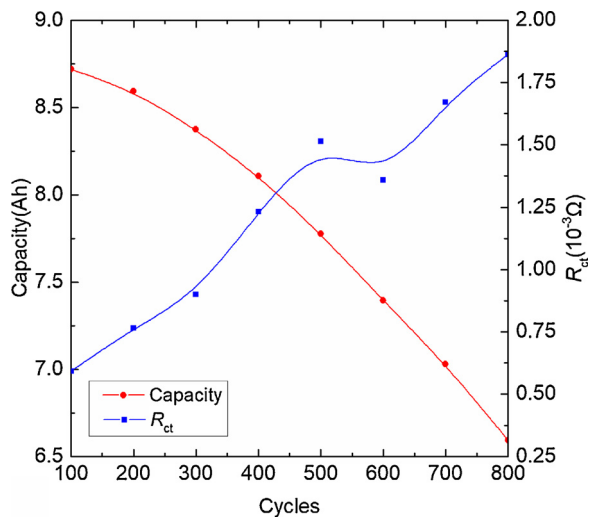


Fig. 11. Comparison of 1C discharge capacity measured at 25°C and charge transfer resistance R_{ct} fitted with impedance spectra measured at 25°C, 50% SOC.

$$\gamma = \frac{R_{ct,0}}{R_{ct}} \quad (24)$$

(3) The corrected calculation model of charge transfer resistance is obtained as Eq. (25).

$$R_{ct}^* = g(T, SOC) = \gamma f(T, SOC) \quad (25)$$

(4) The charge transfer resistance $R_{ct, std}$ at $T_{std} = 298$ K and $SOC_{std} = 0.5$ is calculated with the corrected calculation model as Eq. (26).

$$R_{ct, std} = g(T_{std}, SOC_{std}) \quad (26)$$

Fig. 15 shows the relative error distribution of the converted charge transfer resistance and that obtained by fitting the impedance spectra at the standard state. The charge transfer resistance is converted from the value at any combination state of 278 K–318 K and 10%–90% SOC after different aging cycles. As is seen from the figure, the error of the

converting from different state is less than 30% over a wide range of battery temperature and SOC. At different aging state, the conversion error in the SOC range of 10%–60% and the temperature range of 288 K–308 K can be kept below 10%. The large error at high temperature and high SOC is mainly due to the fact that the arc of the charge transfer resistance in the impedance spectrum is not obvious as shown in Fig. 2(a)(b). The error at low temperatures is mainly due to the fact that the frequency range corresponding to the arc of the charge transfer resistor becomes larger. The precise matching of the charge transfer resistance in the impedance spectrum cannot be achieved within the selected frequency range.

5.3. Estimation of state of health with converted charge transfer resistance

SOH of a fresh battery is defined as 100%. In the paper, the battery after 100 aging cycles is treated as a fresh battery. And the aging of the battery is terminated, i.e. SOH = 0%, when the charge transfer resistance in the standard state increases to three times that of the fresh battery. The charge transfer resistance at the end of battery life is $R_{ct,EOL}$ as Eq. (27). And SOH is defined as Eq. (28).

$$R_{ct,EOL} = 3R_{ct,fresh} \quad (27)$$

$$SOH = \frac{R_{ct,EOL} - R_{ct}}{R_{ct,EOL} - R_{ct,fresh}} \times 100\% \quad (28)$$

Charge transfer resistance R_{ct} is obtained by fitting the measured electrochemical impedance spectra at different temperature, SOC and number of aging cycles with the equivalent impedance model. To verify the method, ten different combinations of temperature and SOC are randomly selected. And the charge transfer resistance at the randomly selected state is converted to the standard state according to the conversion method proposed. The statistical distribution of the charge transfer resistance at the standard state obtained by the conversion is given in the form of a box diagram as Fig. 16. Each "box" reflects the average, median, upper and lower quartiles and extreme statistics of the converted charge transfer resistance. The hollow square in each box represents the average value of the charge transfer resistance converted from ten randomly selected states. For comparison, the black dotted line is the charge transfer resistance R_{ct} obtained by fitting the impedance spectra to the impedance model at the standard state after the same number of aging cycles. It shows that the black dashed line and

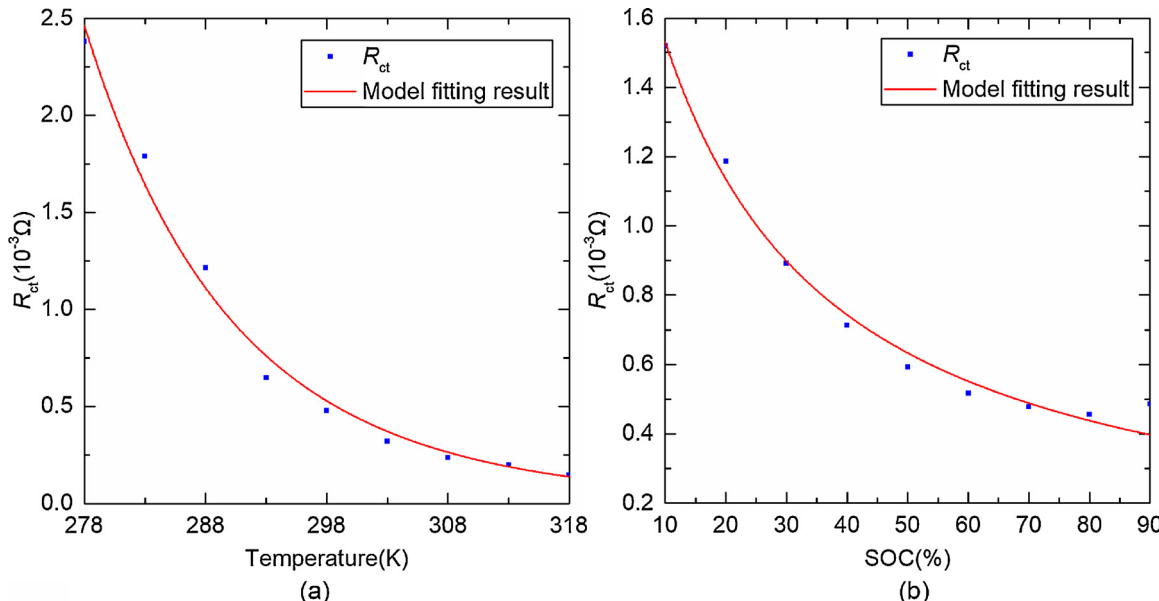


Fig. 12. The charge transfer resistance R_{ct} at different battery state and the relative error of R_{ct} from direct fitting and model calculation.
(a) R_{ct} at different temperature, 70% State of Charge (SOC) and model fitting result; (b) R_{ct} at different SOC, 298 K and model fitting result.

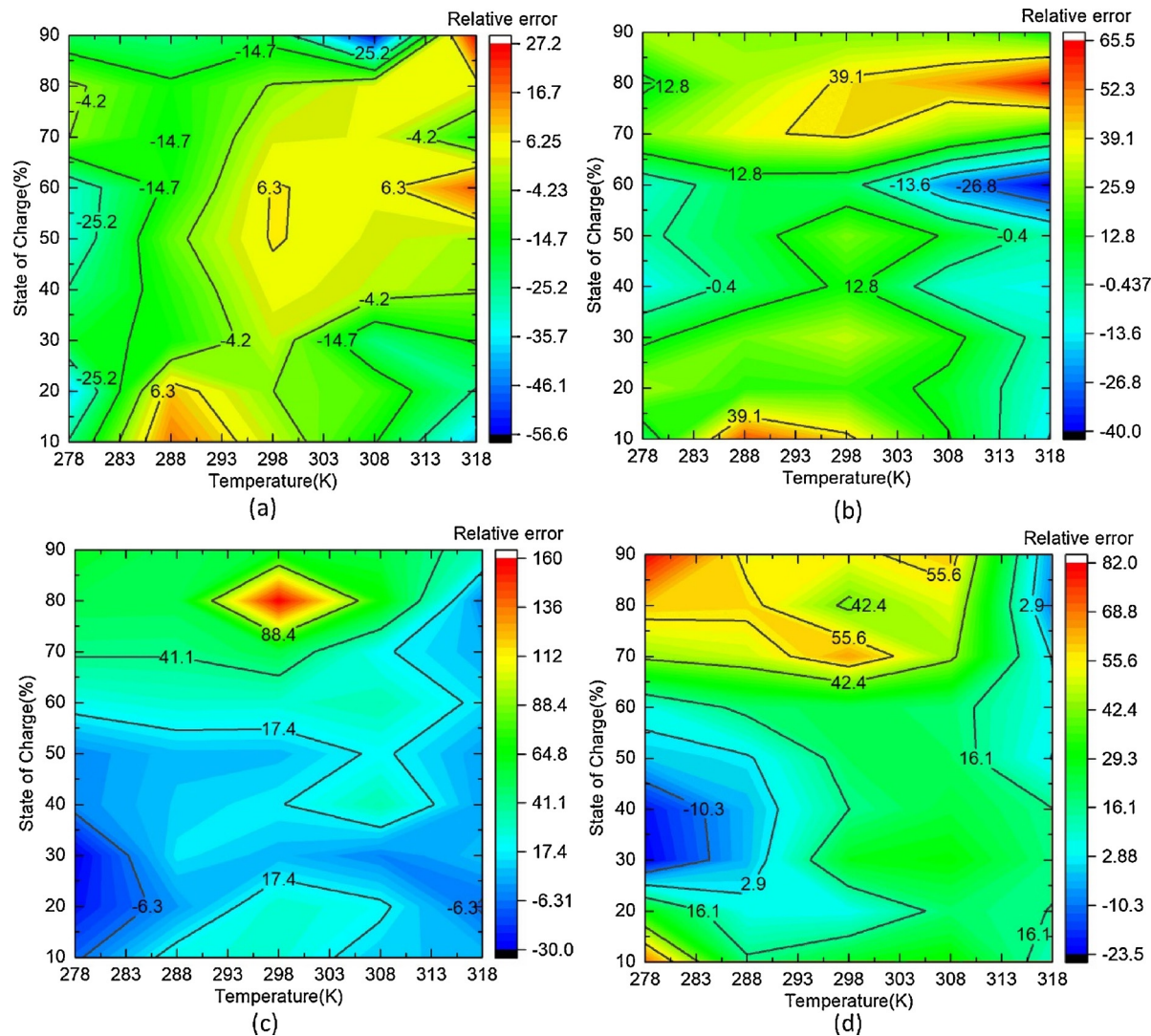


Fig. 13. Relative error between R_{ct} fitted with electrochemical impedance spectra and the results calculated with model at different temperature and State of Charge (SOC), (a) after 100 aging cycles; (b) after 300 aging cycles; (c) after 500 aging cycles; (d) after 700 aging cycles.

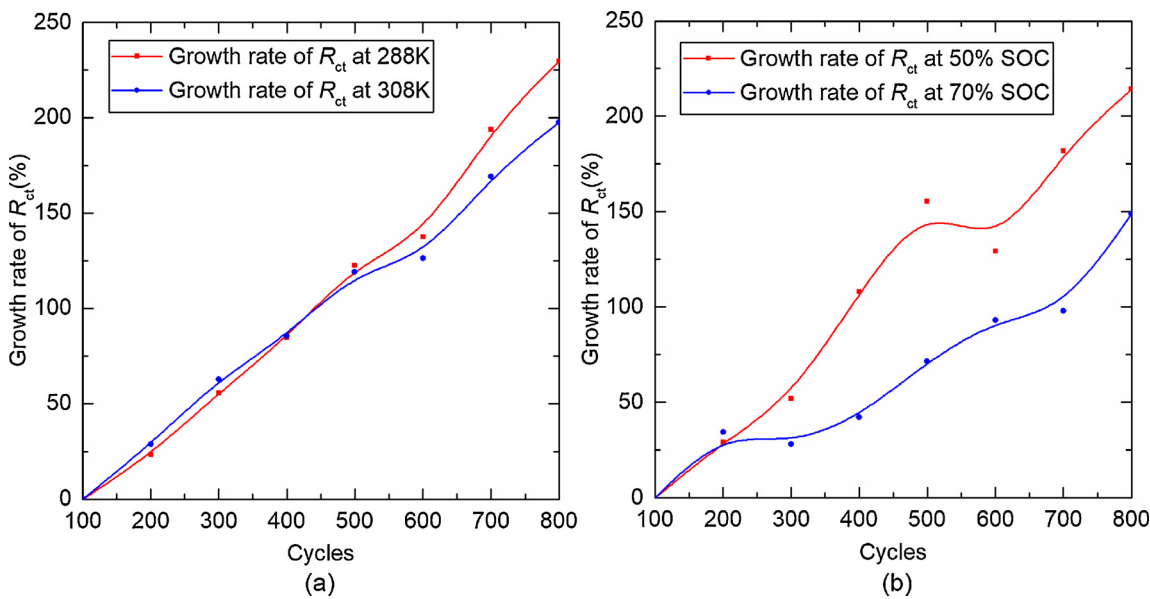


Fig. 14. Growth rate of the charge transfer resistance R_{ct} at different temperature and State of Charge (SOC) after different aging cycles.

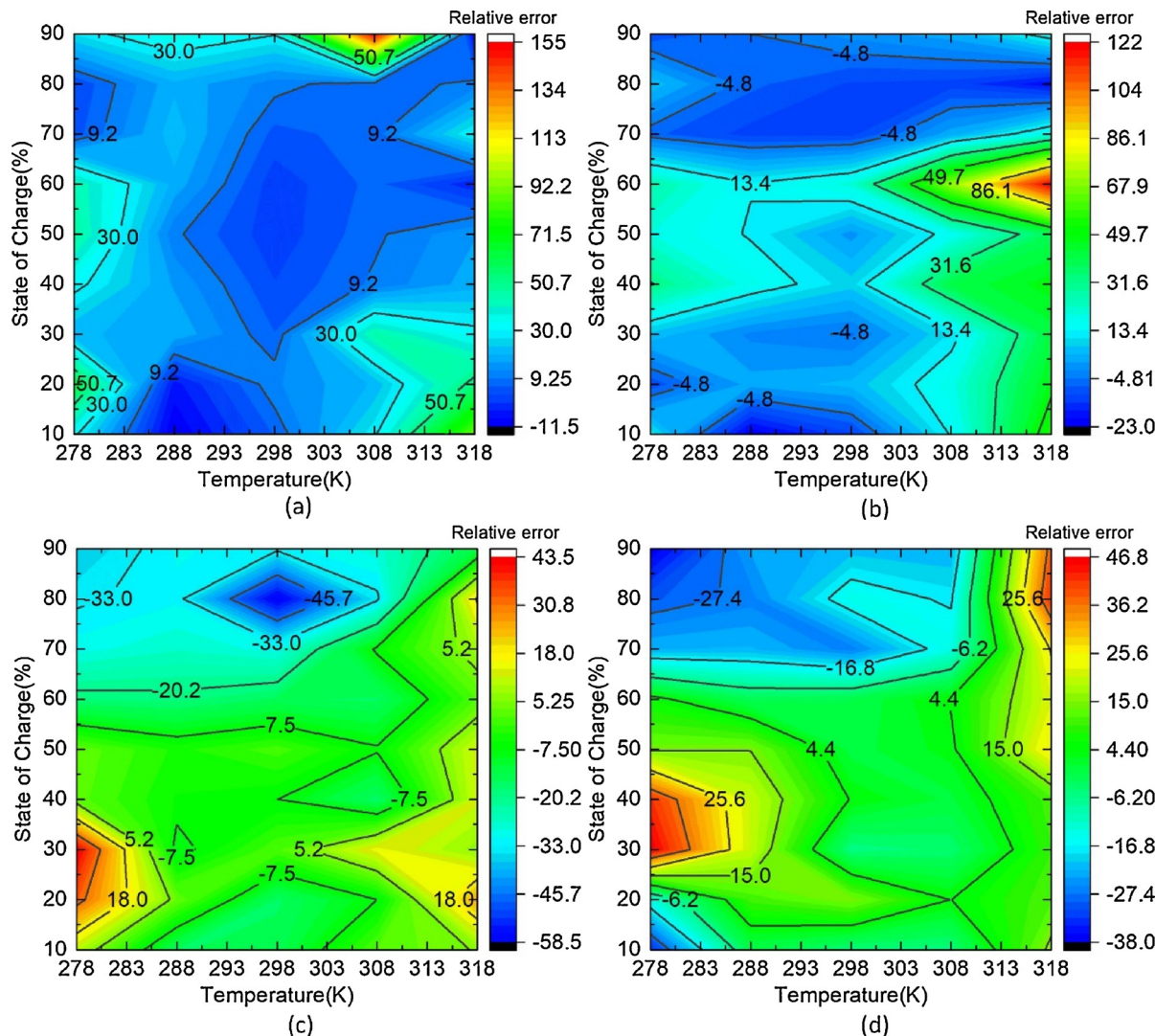


Fig. 15. Relative error between the charge transfer resistance R_{ct} at 298 K, 50% State of Charge (SOC) and the converted charge transfer resistance at standard state $R_{ct, std}$ from different temperature and SOC, (a) after 100 aging cycles; (b) after 300 aging cycles; (c) after 500 aging cycles; (d) after 700 aging cycles.

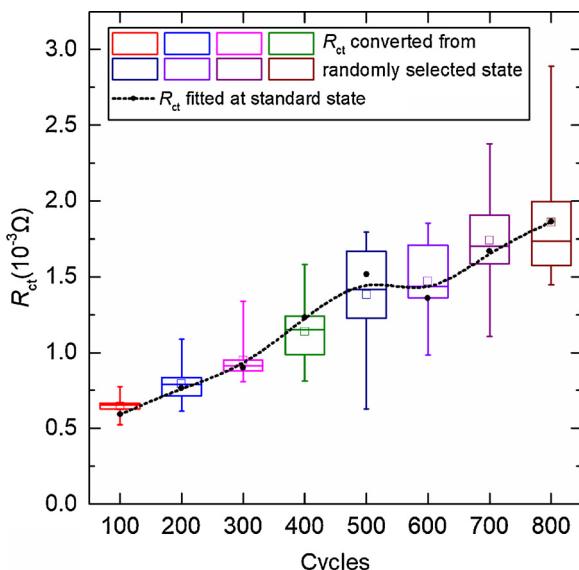


Fig. 16. Box chart of the charge transfer resistance R_{ct} converted from the value at ten randomly selected states after different aging cycles.

the average value shown in the box plot coincide well. The charge transfer resistance conversion method proposed in the paper can remove the effect of temperature and SOC. And the converted charge transfer resistance and the actual value change trend are basically the same. It is feasible to estimate the battery SOH based on the method of the charge transfer resistance conversion.

SOH of the battery is calculated according to Eq. (28) based on the average of the charge transfer resistance converted. Meanwhile, SOH of the battery is also calculated by using the charge transfer resistance obtained by direct fitting. Fig. 17 shows the comparison of the results of the battery SOH curves calculated by the two types of charge transfer resistance. It is seen that SOH of the battery calculated by the two types of charge transfer resistance is quite close. Except the error caused by the large fluctuation of the charge transfer resistance obtained by fitting the impedance spectra between 400 and 600 cycles, the estimation error of SOH at different aging state is acceptable. The absolute error of SOH estimation is less than 15%, and the characterization parameter used to estimate SOH is not limited to being obtained from a particular temperature and SOC. In addition, after the battery has aged to 800 cycles, a negative value of SOH would appear. It means that the charge transfer resistance of the battery becomes three times greater than that of the fresh battery cell. This involves the appropriate value of the charge transfer resistance at the end of the battery life. And it is beyond

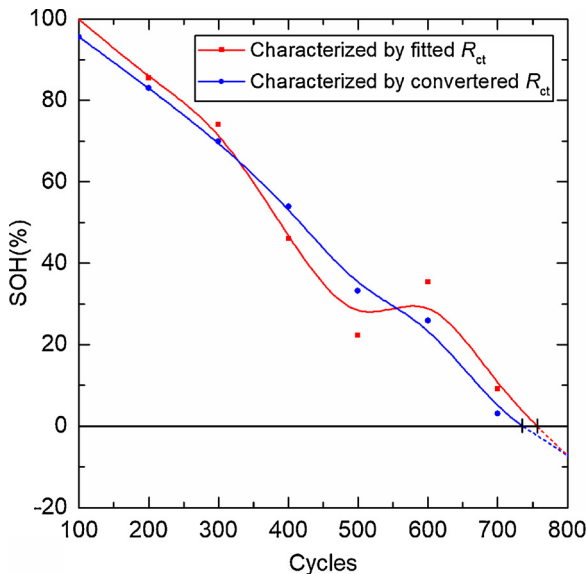


Fig. 17. Comparison of State of Health (SOH) characterized by the charge transfer resistance R_{ct} fitted and converted.

the scope of the paper.

6. Conclusions

In this paper, the effect of temperature and SOC on the impedance spectroscopy of the battery are studied with a series of experiments. A chaotic particle swarm search method is proposed to determine the initial value of the equivalent impedance model parameters for the later optimization. By fitting EIS with the equivalent impedance model, it is found that the charge transfer resistance increases significantly with the aging cycles. Besides, the charge transfer resistance and its growth rate are all affected by temperature and SOC.

In order to estimate SOH, a method to converter the charge transfer resistance at any temperature and SOC to the standard state are proposed and verified. The results show that the uncertainty of the charge transfer resistance obtained by fitting EIS at high SOC and temperature leads to larger error when the conversion is performed. And the conversion error in the SOC range of 10%–60% and the temperature range of 288 K–308 K can be kept below 10%.

With the method, SOH is finally estimated with the charge transfer resistance at a variety of state. It shows that the trends of SOH estimated with the charge transfer resistance at 50% SOC, 298 K and converted from the randomly selected state agree well. It relaxes the requirements of the battery temperature and SOC control for the SOH estimation with the charge transfer resistance and benefits the vehicular applications.

Although the charge transfer resistance at different state is able to be used to estimate SOH with the method proposed in the paper, an easy determining method for the resistance should be studied in the future. Especially for some batteries or at certain state, when the charge transfer resistance cannot be easily observed from the EIS, an alternative method needs to be proposed.

Declarations of interest

None.

CRediT authorship contribution statement

Xueyuan Wang: Conceptualization, Methodology, Software, Validation, Formal analysis, Investigation, Data curation, Writing - original draft, Visualization. **Xuezhe Wei:** Conceptualization, Resources, Writing - review & editing, Supervision, Project administration, Funding acquisition. **Haifeng Dai:** Writing - review & editing, Conceptualization, Supervision.

Acknowledgement

This work is financially supported by the National Natural Science Foundation of China (NSFC, Grant number is U1764256).

References

- [1] D. Andre, A. Nuhic, T. Soczka-Guth, D.U. Sauer, Eng. Appl. Artif. Intell. 26 (2013) 951–961.
- [2] H.-T. Lin, T.-J. Liang, S.-M. Chen, IEEE Trans. Industr. Inform. 9 (2013) 679–685.
- [3] Z. Chen, C.C. Mi, Y. Fu, J. Xu, X. Gong, J. Power Sources 240 (2013) 184–192.
- [4] M. Berecibar, I. Gandida, I. Villarreal, N. Omar, J. Van Mierlo, P. Van den Bossche, Renew. Sustain. Energy Rev. 56 (2016) 572–587.
- [5] A. Guha, A. Patra, Ieee Trans. Transp. Electrific. 4 (2018) 135–146.
- [6] M. Zhu, W. Hu, N.C. Kar, in: Transportation Electrification Conference and Expo, (2016), pp. 1–6.
- [7] P. Sobana, K. Ramesha, Csi Trans. ICT 4 (2016) 23–28.
- [8] D.D. Macdonald, Electrochim. Acta 51 (2006) 1376–1388.
- [9] Y. Xie, J. Li, C. Yuan, Electrochim. Acta 127 (2014) 266–275.
- [10] M. Xiao, S.-Y. Choe, J. Power Sources 277 (2015) 403–415.
- [11] J.G. Zhu, Z.C. Sun, X.Z. Wei, H.F. Dai, J. Power Sources 274 (2015) 990–1004.
- [12] U. Westerhoff, T. Kroker, K. Kurbach, M. Kurat, J. Energy Storage 8 (2016) 244–256.
- [13] H.F. Yuan, L.R. Dung, IEEE Transactions on Vehicular Technology, PP, (2017) 1–1.
- [14] D.I. Stroe, M. Swierczynski, A.I. Stan, V. Knap, R. Teodorescu, S.J. Andreasen, IEEE Energy Conversion Congress and Exposition (ECCE), (2014), pp. 4576–4582.
- [15] M. Galeotti, L. Cina, C. Giannamico, S. Cordiner, A. Di Carlo, Energy 89 (2015) 678–686.
- [16] L.H.J. Rajmakers, K.M. Shivakumar, M.C.F. Donkers, M.J.G. Lammers, H.J. Bergveld, IFAC-PapersOnLine 49 (2016) 42–47.
- [17] L.H.J. Rajmakers, D.L. Danilov, J.P.M. van Lameren, M.J.G. Lammers, P.H.L. Notten, J. Power Sources 247 (2014) 539–544.
- [18] W.X. Huang, J.A. Abu Qahouq, Ieee Trans. Ind. Electron. 61 (2014) 5987–5995.
- [19] T.T. Nguyen, V.L. Tran, W.J. Choi, Ieee, Ieee 23rd International Symposium on Industrial Electronics (Isie) 2014 (2014) 454–458.
- [20] X. Wei, X. Wang, H. Dai, Energies 11 (2018) 64.
- [21] J.A.A. Qahouq, Z. Xia, IEEE Transactions on Industrial Electronics, PP, (2017) 1–1.
- [22] T. Yokoshima, D. Mukoyama, H. Nara, S. Maeda, K. Nakazawa, T. Momma, T. Osaka, Electrochim. Acta 246 (2017) 800–811.
- [23] Y. Hoshi, N. Yakabe, K. Isobe, T. Saito, I. Shitanda, M. Itagaki, J. Power Sources 315 (2016) 351–358.
- [24] R. Al Nazer, V. Cattin, P. Granjon, M. Montaru, M. Ranieri, Ieee Trans. Veh. Technol. 62 (2013) 2896–2905.
- [25] D.A. Howey, P.D. Mitcheson, V. Yufit, G.J. Offer, N.P. Brandon, Ieee Trans. Veh. Technol. 63 (2014) 2557–2566.
- [26] N. Lohmann, P. Haussmann, P. Wesskamp, J. Melbert, T. Musch, Sae Int. J. Altern. Powertrains 4 (2015) 308–317.
- [27] C.T. Hsieh, C.T. Pai, Y.F. Chen, P.Y. Yu, R.S. Juang, Electrochim. Acta 115 (2014) 96–102.
- [28] Q.C. Zhuang, J.M. Xu, X.Y. Fan, Q.F. Dong, Y.X. Jiang, H. Ling, S.G. Sun, Chin. Sci. Bull. 52 (2007) 1187–1195.
- [29] D. Andre, M. Meiler, K. Steiner, C. Wimmer, T. Soczka-Guth, D.U. Sauer, J. Power Sources 196 (2011) 5334–5341.
- [30] P. Gao, C.F. Zhang, G.W. Wen, J. Power Sources 294 (2015) 67–74.
- [31] C.-C. Yang, J.-H. Tang, J.-R. Jiang, Appl. Energy 162 (2016) 1419–1427.
- [32] M. Balasundaram, V. Ramar, C. Yap, L. Li, A.A.O. Tay, P. Bayala, J. Power Sources 328 (2016) 413–421.
- [33] H.-M. Cho, Y.J. Park, J.-W. Yeon, H.-C. Shin, Electron. Mater. Lett. 5 (2009) 169–178.
- [34] R. Pauliukaita, M.E. Ghica, O. Fatibello-Filho, C.M.A. Brett, Electrochim. Acta 55 (2010) 6239–6247.
- [35] Q.K. Wang, Y.J. He, J.N. Shen, X. Hu, Z.F. Ma, IEEE Transactions on Power Electronics, PP, (2017) 1–1.
- [36] X.-Z. Liao, Z.-F. Ma, Q. Gong, Y.-S. He, L. Pei, L.-J. Zeng, Electrochim. Commun. 10 (2008) 691–694.
- [37] F. Gao, Z. Tang, Electrochim. Acta 53 (2008) 5071–5075.
- [38] S.H. Ye, J.K. Bo, C.Z. Li, J.S. Cao, Q.L. Sun, Y.L. Wang, Electrochim. Acta 55 (2010) 2972–2977.
- [39] S.E. Li, B. Wang, H. Peng, X. Hu, J. Power Sources 258 (2014) 9–18.
- [40] M. Ausloos, M. Dirickx, Springer Berlin, volume 264 (2006) 222–225(224).
- [41] S.S. Zhang, K. Xu, T.R. Jow, J. Power Sources 160 (2006) 1403–1409.
- [42] S.S. Zhang, J. Power Sources 161 (2006) 1385–1391.

- [43] R. Li, J. Wu, H. Wang, G. Li, *Ind. Electron. Appl.* (2010) 684–688.
- [44] U. Westerhoff, T. Kroker, K. Kurbach, M. Kurrat, *J. Energy Storage* 8 (2016).
- [45] J. Huang, Z. Li, J. Zhang, *J. Power Sources* 273 (2015) 1098–1102.
- [46] M. Guo, G. Sikha, R.E. White, *J. Electrochem. Soc.* 158 (2011) A122–A132.
- [47] C. Pastor-Fernández, K. Uddin, G.H. Chouchelamane, W.D. Widanage, J. Marco, *J. Power Sources* 360 (2017) 301–318.
- [48] L. Chen, Z. Lü, W. Lin, J. Li, H. Pan, *Measurement* 116 (2018) 586–595.
- [49] S.B. Lee, S.I. Pyun, *Carbon* 40 (2002) 2333–2339.
- [50] M. Dollé, S. Gruegeon, B. Beaudoin, L. Dupont, J.M. Tarascon, *J. Power Sources* 97–98 (2001) 104–106.
- [51] C. Huang, K. Huang, H. Wang, S. Liu, Y. Zeng, *J. Solid State Electrochem.* 15 (2011) 1987–1995.
- [52] H. Wang, *New Chemical Materials* (2006).
- [53] M.B. Pinson, M.Z. Bazant, *J. Electrochem. Soc.* 160 (2013) A243–A250.
- [54] R. Srinivasan, B.G. Carkhuff, M.H. Butler, A.C. Baisden, *Electrochim. Acta* 56 (2011) 6198–6204.
- [55] G. Nagasubramanian, *J. Power Sources* 87 (2000) 226–229.